Supplementary information

Interplay of vibrational wavepackets during an ultrafast electron transfer reaction

In the format provided by the authors and unedited

Interplay of vibrational wavepackets during an ultrafast electron transfer reaction

Shahnawaz R. Rather, Bo Fu, Bryan Kudisch, Gregory D. Scholes*

Department of Chemistry
Princeton University, Princeton NJ 08544 USA
*Correspondence to: gscholes@princeton.edu

Supplementary Information

Table of Contents

Experimental Methodology

Materials and sample preparation. *N*, *N*'-Bis(2,6-methylphenyl)-3,4,9,10-perylenetetracarboxylic diimide (PDI), dimethylaniline (DMA), diethylaniline (DEA) were purchased from Sigma-Aldrich. Tetrahydrofuran (THF), unstabilized and HPLC grade was purchased from EMD Millipore sold under the tradename Omnisolv Tetrahydrofuran. The solvents were of HPLC grade and used without further purification. DMA and DEA were stored in sure/sealed bottles.

The chemically reduced PDI was generated by treating PDI with tetrakis(diethylamino)ethylene (TDAE) in THF solvent. TDAE was purchases from Sigma-Aldrich. PDI anion was generated by gradually adding TDAE to the PDI solution in THF, and the conversion was monitored by tracking the absorption spectra of the solution. The gradual addition of TDAE resulted in the disappearance of PDI absorption (peaked at around 520 nm) and the appearance of PDI anion absorption (peaked at around 710 nm). The addition was continued until all PDI converted into PDI anion.

The sample solutions of PDI in DMA or DEA and chemically reduced PDI were transferred to sealed cuvettes and purged with nitrogen for about 30 minutes to remove any trace amounts of oxygen. The concentration of all the PDI solutions were maintained in a limit to avoid any aggregation. The concentration was chosen to provide an optical density of 0.3-0.4 in a 1 mm pathlength cuvette. In this range of optical density, the absorption and fluorescence spectra do not show any peak shift or change in the shape of the spectra, thereby eliminating any possibility of aggregation.

Broadband pump-probe spectroscopy. A detailed account of the pump probe setup can be found in Mcclure et al[1]. Briefly, a 80 fs, 800 nm laser light at a repetition rate of 5 kHz from a Ti:sapphire seeded regenerative amplifier (Coherent Libra) was used to pump a home-built noncollinear optical parametric amplifier (NOPA) and thereby generate a desired pulse spectrum, which is resonant with PDI electronic absorption. The NOPA output was sent into a folded grating compressor and then into a two-prism compressor to compress the pulses down to temporal bandwidth of 15 fs as estimated with polarization-gated frequency resolved optical gating (PG-FROG) in broadband pump−probe experiments. The PG-FROG profile of a NOPA pulse used in BBPP measurements of PDI in THF, dimethylaniline, and diethylaniline in the spectral range of 17800 – 21200 cm^{-1} is shown in Fig. 1.

The compressed output was collimated in a reflective telescope and then split into three beams by a wedge beam splitter. Out of the three beams, the two beams reflected from the front and back surfaces of the wedge, having less than 1% total intensity, were used as a reference and probe beams. The transmitted beam was used as a pump beam. The time delay between the pump and the probe beams was controlled by means of an electronically controlled translation stage in the pump path, which was scanned in 4 fs steps for the 5 ps time window. The BBPP data of each sample shown in this work is the average of 10-20 separate scans. Each scan was averaged for 400 pump on-pump off pulse pairs, and each pump on-pump off pulse pair was integrated over 4 pulses each. The pump power was kept at around 50 µW, which corresponds to a pulse energy of 10 nJ/pulse. In the range of pump power, the transient absorption signal was linear with pump intensity and sample concentration. The transient signals were measured with pump and probe polarization set parallel to each other. The magnitude of wavepacket oscillations is always higher with parallel polarization of the pump and probe beams.

The measurements were performed under two configurations.

1. **Degenerate pump and probe pulses.** Under this configuration, an exact replica of the pump pulse was used as a probe pulse for measuring the transient absorption signal. Both pump and probe pulses have same time-duration. The pulse was characterized using PG-FROG technique in a 1 mm

thick glass cuvette filled with tetrahydrofuran or dimethylaniline solvent. The measurements of the samples were also carried out in 1 mm thick cuvette.

2. Nondegenerate pump and probe pulses. Under this configuration, the pump pulse is a compressed NOPA output, but the probe pulse is not a replica of the pump pulse. The probe pulse is a white light spectrum generated directly by focusing the 800 nm laser light on a 2 mm thick sapphire crystal. The advantage of using white light spectrum from a sapphire in comparison to using a replica of the pump pulse is the broader bandwidth offered by the white light. For example, when pump pulse is resonant with PDI in THF or DMA, its bandwidth ranges from $17800 - 21200$ cm^{-1}. So, to capture the coherent dynamics outside this spectral region demands a broader bandwidth, which was provided by white light spectrum ($13000 - 22000$ cm^{-1}) from the sapphire crystal. Given that PDI in THF and DMA has excited state absorption and product absorption signal in the $13000 - 18000$ cm^{-1} region, white light spectrum provides the full bandwidth to access to those transient signals. To enable a better resolution of the white light outside the pump spectral region, a thinner cuvette of 100 μm pathlength was used. In addition, the white light from the sapphire was also compressed by a pair of chirped mirrors. The best resolution under our experimental conditions was obtained by using 7 passes between the two chirped mirrors. More details about using white light from sapphire as a probe pulse for measurement of oscillations can be found in the work of Liebel et al[2].

BBPP coherent spectroscopy was also carried out for the chemically produced PDI anion, which absorbs in the $13000 - 16000$ cm^{-1} region. For these measurements, the NOPA spectrum was shifted to cover the absorption region. The NOPA spectrum was again compressed to ca. 15 fs. For this sample of PDI anion in THF, the measurements were again performed under degenerate and nondegenerate configurations.

The post-acquisition data analysis involves removal of dynamic scatter contributions that appears as spectrally resolved fringes on each transient spectra- owing to broad bandwidth of the pump pulse. This scatter was filtered by performing an inverse Fourier transform (FT) of the spectra at each time delay, which transforms the frequency domain data into time domain. In the time-domain, a super-Gaussian filter was applied over the signal with a fixed bandwidth, which selectively filters out the dynamic scatter. A fast Fourier transform of the scatter free time-domain signal converts the data back to the frequency domain. This is followed by fitting of the population dynamics using exponentials as described previously[3]. The fitted exponential traces are then subtracted from the raw traces to remove the population dynamics contributions and thereby obtain oscillatory components as residuals at each probe frequency.

Given that the broad pump laser pulse accesses Franck-Condon active vibrations by creating superposition of vibrational levels, that produce oscillations in the time domain transient signals of the electronic states. The time-domain oscillatory signals at each probe frequency are therefore Fourier transformed to convert the periodic oscillations into their corresponding frequency. The frequency of the oscillations corresponds to the frequency of the Franck-Condon active modes. The Fourier transform information is either presented in the form of either probe-frequency–Fourier transformed frequency map or as integrated Fourier transformed spectra in specific transient absorption signals.

The work reported here also relies on coherent vibrational dynamics of individual frequency components, which is obtained by filtering out the desired frequency band using super-Gaussian filters of finite width. We have also relied on using time-domain filters, where in a time-domain formulation of a 'Tuckey' window is convoluted with the raw residual traces to selectively obtain the vibrational dynamics of a specific frequency/Franck-Condon active mode. All the analyses reported here were performed in Matlab.

Resonance-Raman measurements: Resonance-Raman measurements were performed on a Horiba Raman spectrometer situated at Imaging and Analysis Center (IAC) in the Princeton Institute for the Science and Technology of Materials (PRISM), Princeton University. A highly monochromatic excitation source of central wavelength 533 nm – resonant with the electronic absorption of PDI in dimethylaniline – was used to obtain a resonance-Raman spectrum. The laser light is focused by a 10X objective on a sample placed over a movable stage. The resulting Raman signal is collected by the same objective and then directed to a grating which diffracts the signal on a camera. Due to significantly large quantum yield of PDI in THF, the Raman signal was overwhelmed by the fluorescence and thus making it impossible to collect the Raman spectrum of PDI in THF. Due to the fluorescence quenching of PDI by dimethylaniline, we were able to record a Raman spectrum of PDI in DMA with strong signal to noise ratio

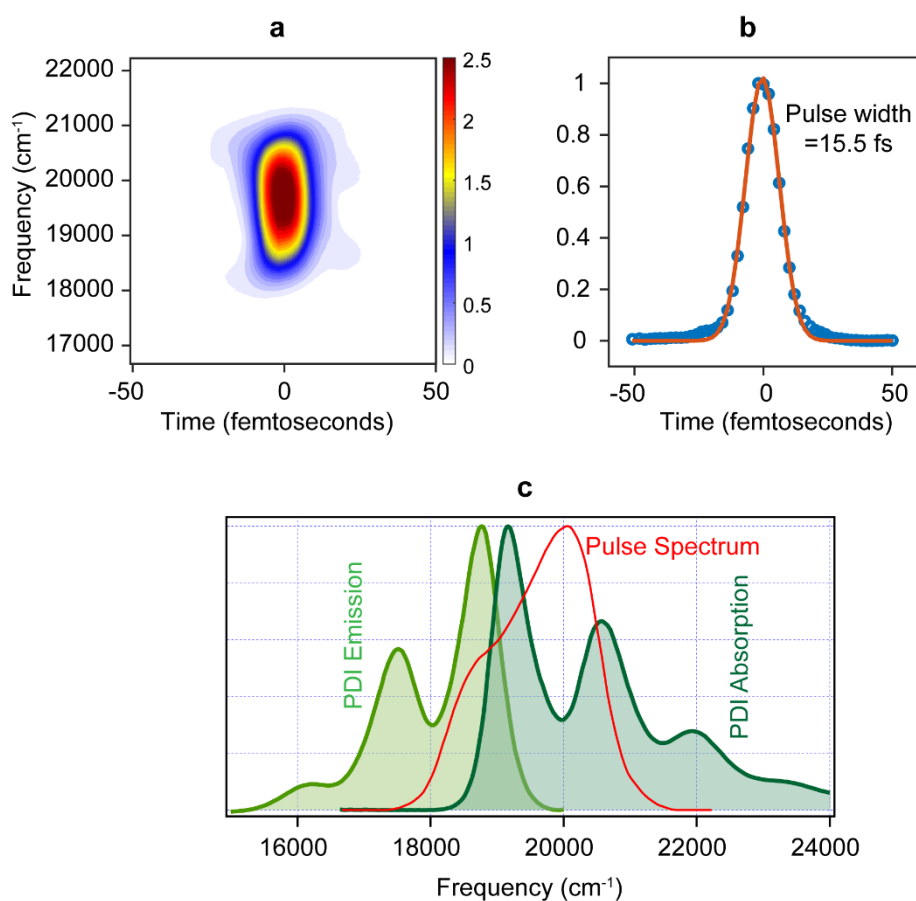**Figure 1| Laser pulse spectrum. a,** A frequency-time map of the laser pulse used for broadband pump-probe spectroscopy of PDI in various solvent environments. **b,** A time domain representation of the compressed pulse spectrum having a full-width-half-maximum of 15.5 femtoseconds. **c,** The pulse spectrum is overlaid on the absorption and emission spectra of PDI in THF.
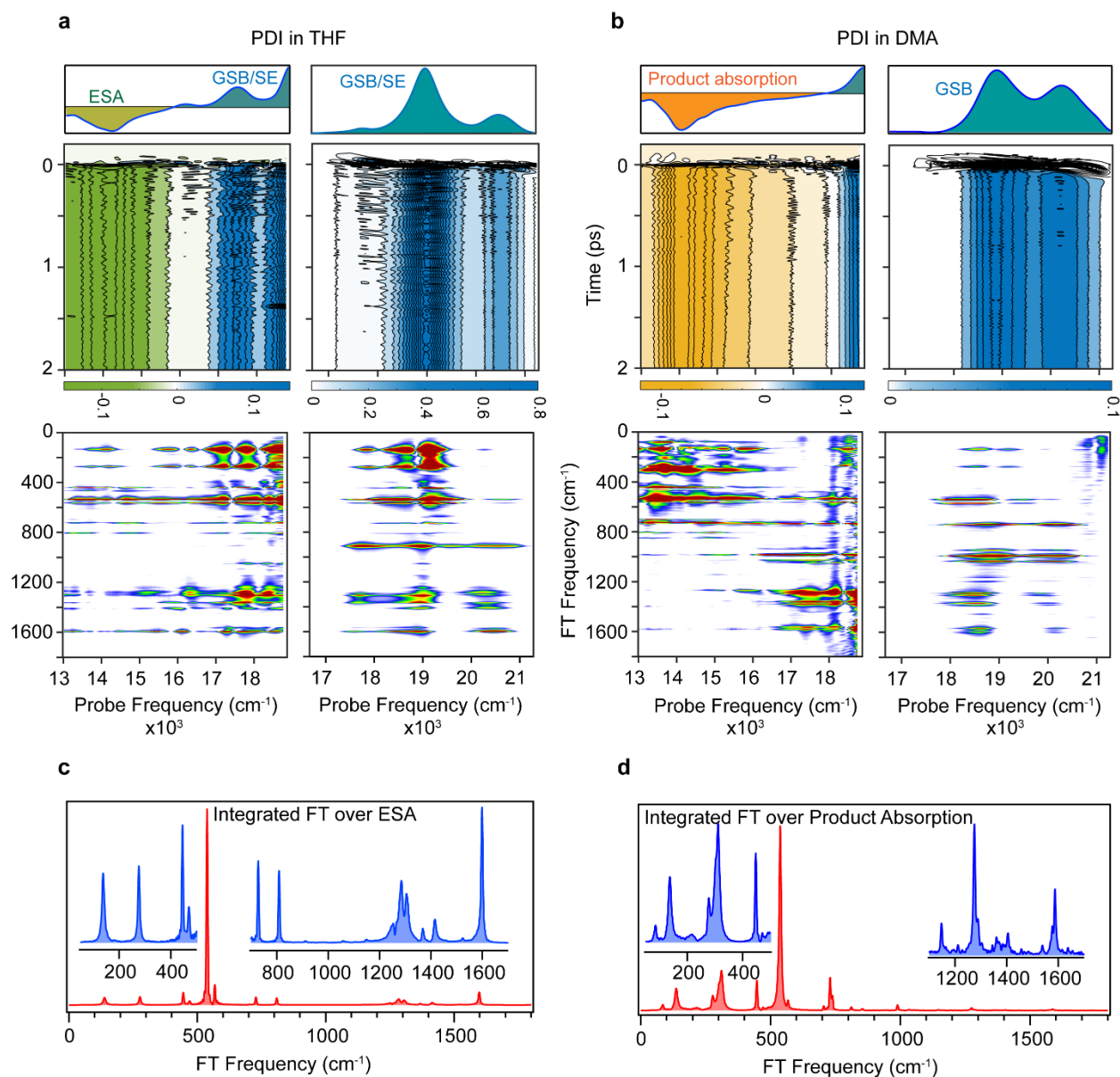
Figure 2| Coherent dynamics during electron transfer reaction. a-b, Wavepacket modulated transient absorption signals of PDI in inert THF and in electron donating DMA media, with the representative transient absorption spectra shown at the top. The bottom panel represent the corresponding Fourier transform maps, which are already shown as a part of figure 1 in the main manuscript. These plots are reproduced here to highlight the stepwise analysis from the raw oscillatory time-domain data to the Fourier transform maps. Also, these plots are presented here in a rainbow color scheme contrary to the different color scheme used in the main manuscript. **c-d**, Integrated Fourier transform spectra of PDI-THF excited state absorption transient signal and PDI-DMA product absorption signal. The blue colored insets are parts of the Fourier transform spectra that are rescaled along the y-axis for clear visualization.
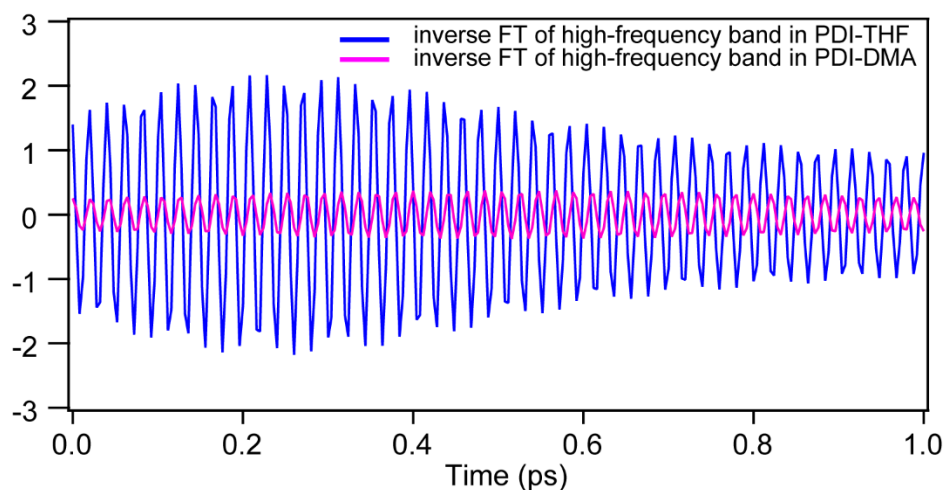
Figure 3| Dephasing of the high-frequency vibrational coherences. Reconstruction of the vibrational wavepacket dynamics of frequencies in the 1550 - 1650 cm^{-1} region of PDI-THF (blue trace) and PDI-DMA (pink trace) data, The reconstruction was carried out by applying time-domain filters to selectively isolate the above mentioned frequency band. The comparison of the oscillation amplitudes highlights the strong contribution of the 1599 cm^{-1} vibrational coherence in the reactant state and its absence in the product state due to enhanced dispersion of the coherence introduced by the electron transfer. Note that, 1599 cm^{-1} band is completely absent in the product state and the oscillations shown as the pink trace correspond to the remainder spectator frequencies 1570 and 1587 cm^{-1} in that spectral region.
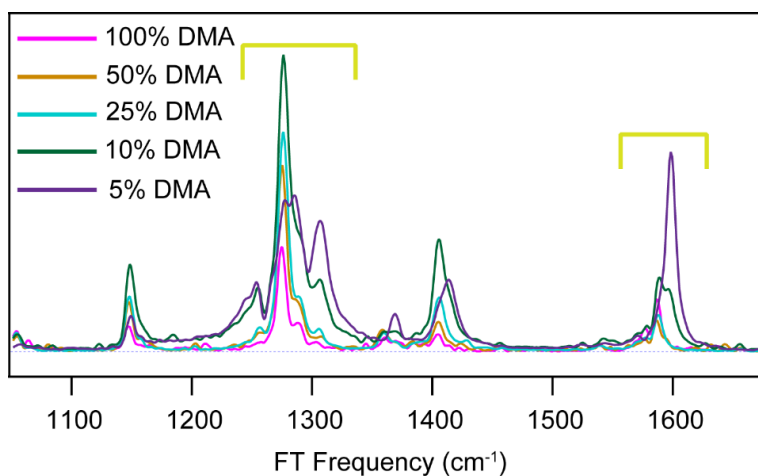
Figure 4| Attenuation of the high-frequency Fourier transform peaks upon dilution of DMA with THF. The integrated FT of the transient absorption signals in the probe frequency region from $13000 - 16000$ cm^{-1} are shown as a function of systematic dilution of DMA with THF. In 100% DMA, this spectral region contains product state absorption signal. Upon dilution, the ET rate slows down, resulting in slow decay of ESA signal of PDI and slow appearance of the product absorption signal. As evident, the FT of the 5% mixture resembles more to the ESA signal of PDI-THF. Overall, the trend shows that with increasing rate of the ET reaction, a few high-frequency vibrational coherences (especially 1599 and 1308 cm^{-1}) lose significant amplitude due to loss of phase coherence.

A Detailed Description of Control Experiments

The coherence analysis of the PDI-DMA reactive system reveals a remarkable feature in the form of a newly produced wavepacket which oscillates at 313 cm^{-1} frequency. In the state-of-the-art coherence experiments, wavepacket are generated by the ultrashort and broadband laser pulses under resonant or non-resonant conditions, the question that naturally arises is about the mechanism by which this new wavepacket is generated. In other words, is this new wavepacket generated by the laser pulse like every other wavepacket, or is it generated by any other means?

The newly produced wavepacket with frequency of 313 cm^{-1} in the reactive PDI-DMA system do not have a counterpart in the nonreactive PDI-THF system. To put it in perspective, both systems share all the frequencies in the low-frequency region like 138, 276, 445, and 538 cm^{-1} except for the 313 cm^{-1} frequency which is solely observed in PDI-DMA. The shared frequencies are observed in the ground state bleach, stimulated emission, and excited state absorption transient signals of PDI-THF; as well as in the excited state absorption of PDI-DMA system (Fig. 5a). However, the 313 cm^{-1} is observed in the PDI-DMA excited state absorption, henceforth termed as product absorption, signal only. The commonality of the wavepacket frequencies between the reactive and nonreactive systems indicate that such wavepackets are generated along the Franck-Condon active modes of PDI by the laser pulse. While as, the new 313 cm^{-1} wavepacket observed in the PDI-DMA product absorption signal is not an outcome of the Franck-Condon excitation of its corresponding mode. In other words, 313 cm^{-1} mode is not a Franck-Condon active mode in PDI.

The 313 cm^{-1} wavepacket is also not an outcome of the Franck-Condon excitation of its corresponding mode in the PDI radical anion that was produced by chemical reduction. PDI radical anion is one of the two products of forward electron transfer reaction between PDI and DMA, the other being DMA cation. In the PDI-DMA system, the product signal appears in 13000 – 18000 cm^{-1} spectral window, and it is this spectral signal that is modulated by the 313 cm^{-1} wavepacket. This spectral signal is characteristic of PDI radical anion absorption, as is previously know, as well as demonstrated by us by chemically reducing PDI to PDI radical anion, whose absorption spectrum is shown in figure 1 of the main manuscript. The coherence measurements of chemically reduced PDI was performed under resonant conditions. The Fourier transform (FT) map and the corresponding integrated Fourier transform are shown in Fig. 5b-c. The frequency analysis indicates that no wavepacket with a frequency of 313 cm^{-1} can be observed in the ground state bleach and excited state absorption signals of PDI radical anion. This control experiment proves that wavepacket of frequency 313 cm^{-1} is not a Franck-Condon active mode in chemically reduced PDI.

The prospect of 313 cm^{-1} wavepacket being a result of ground state complexation between electron acceptor PDI and electron donor DMA was also ruled out. Firstly, if the ground state complexation between PDI and DMA activates a Franck-Condon intermolecular mode, then it is highly likely that the coherent oscillations corresponding to that mode would appears in the ground state bleach signal of the PDI-DMA system, like we observe for every other mode. The ground state bleach signal of PDI-DMA system does not show any peak at 313 cm^{-1} frequency (Fig. 5d). Secondly, resonance-Raman measurements of PDI-DMA system performed with resonant pumping by 530 nm excitation laser source produce a Raman spectrum which completely matches with the Fourier transform spectrum of the ground state bleach signal (Fig. 5e). All the frequencies that appears in the ground state bleach signal of PDI-DMA are also observed in the resonance-Raman spectrum. No peak with a frequency of 313 cm^{-1} was observed in the resonance-Raman spectrum, which indicates that even if this mode may be a normal mode of PDI-DMA system, but it is neither Raman active nor Franck-Condon active. These measurements, therefore, rule out the origins of the newly produced 313 cm^{-1} frequency as a result of ground state complex formation between PDI and DMA.

In summary, all of these control experiments and data analysis suggest that the newly produced 313 cm^{-1} wavepacket is not an outcome of Franck-Condon excitation of its corresponding mode in the reactant state, instead it is generated by the ultrafast electron transfer reaction itself (Scheme 1).
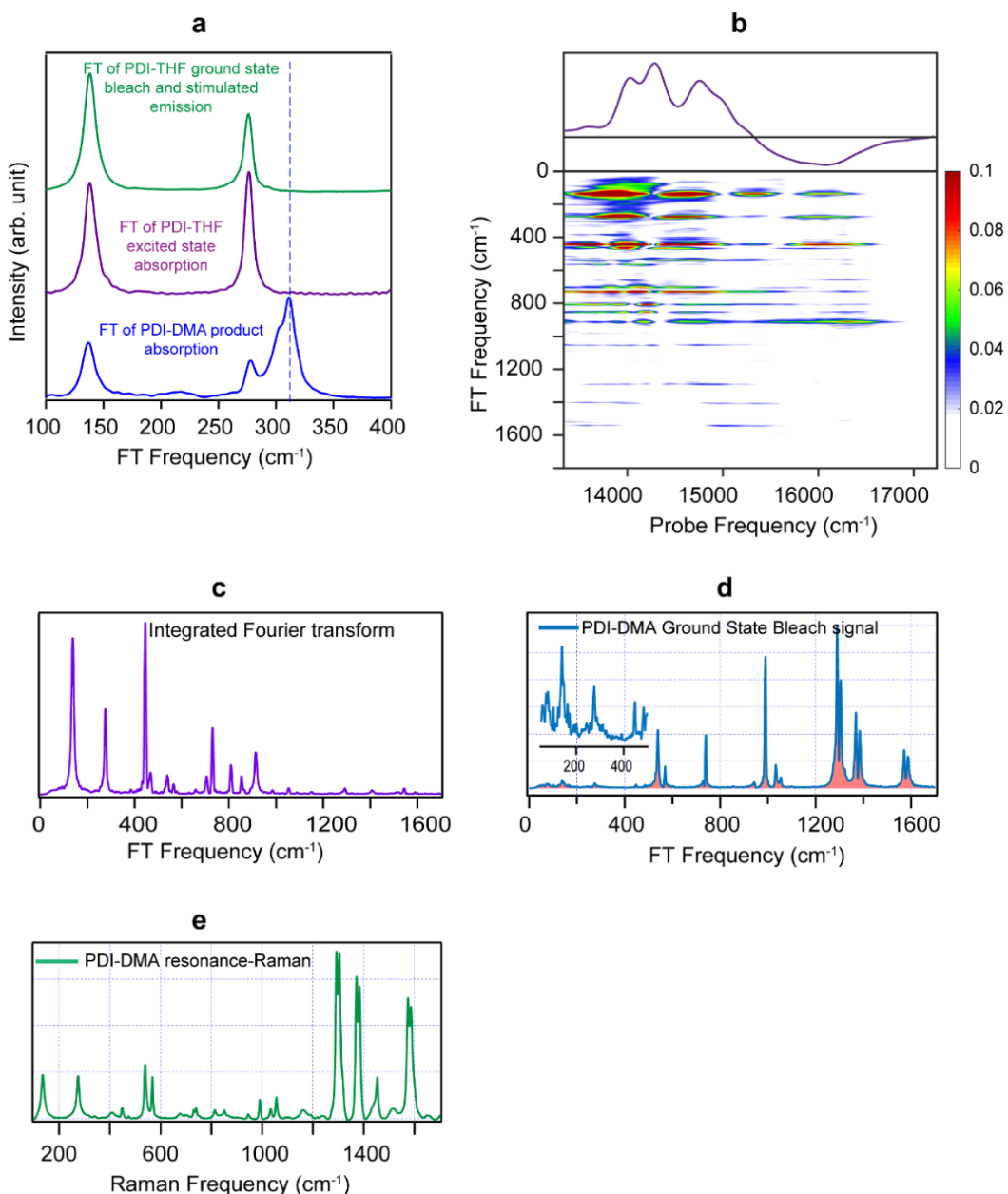

Figure 5| Experimental data in support of the Electron transfer induced vibrational coherence. a, The three spectra show the comparion of the integrated Fourier transforms in the PDI-DMA product absorption, PDI-THF excited state absorption, and PDI-THF ground state bleach/stimulated emission signals. **b,** The FT frequency – probe frequency map obtained by Fourier transformation of the wavepacket oscillations of transient absorption signals of PDI radical anion. **c,** The integrating FT spectrum of the map in the above plot. **d,** Integrated FT in the ground state bleach transient signal of PDI-DMA reactive system. **e,** The resonance-Raman of PDI-DMA obtained at 533 nm excitation is shown, highlighting the absence of 313 cm^{-1} frequency in this spectrum. Some of the spectra used in this figure are also a part of Figure 2 in the main manuscript. They are reproduced here to provide more discussion to the origin of the new vibrational coherence.
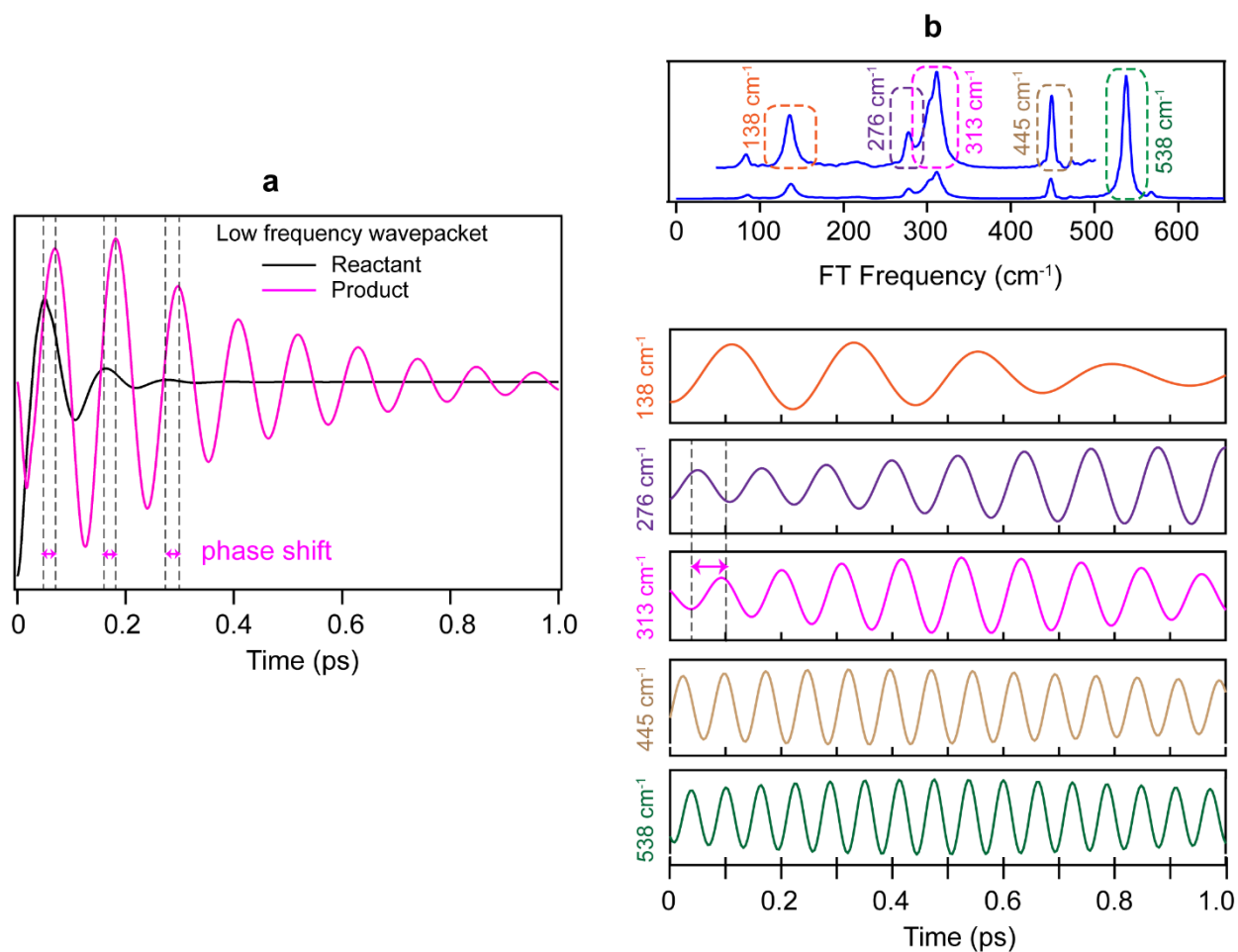
Figure 6| Phase analysis of the multi-peaked, impulsively generated coherence. a, Simulated wavepacket dynamics of the low-frequency mode generated impulsively by the electron transfer reaction on the product state (pink trace) when the reactant state is prepared coherently along both high- and low-frequency modes. The black colored trace is the wavepacket dynamics of the low-frequency wavepacket on the reactant state. Note the phase-shift between the two traces that originates from the electron transfer being ballistically promoted by the high-frequency mode. **b,** Coherent vibrational dynamics of individual frequency components of 138, 276, 313, 445, and 538 cm^{-1} frequencies is reconstructed upon applying a time-domain Tuckey window bandpass filter to the experimental obtained data. The filtered time-traces are drawn up to 1 ps to distinctly see the initial phase of the oscillations. Notice the shift in the initial phase of the 313 cm^{-1} coherence relative to all other spectator coherences, indicative of its generation by the electron transfer reaction itself. Plot a in this figure is also a part figure 3 in the main manuscript, and used here for comparison with the experimentally obtained phase of the vibrational coherences.
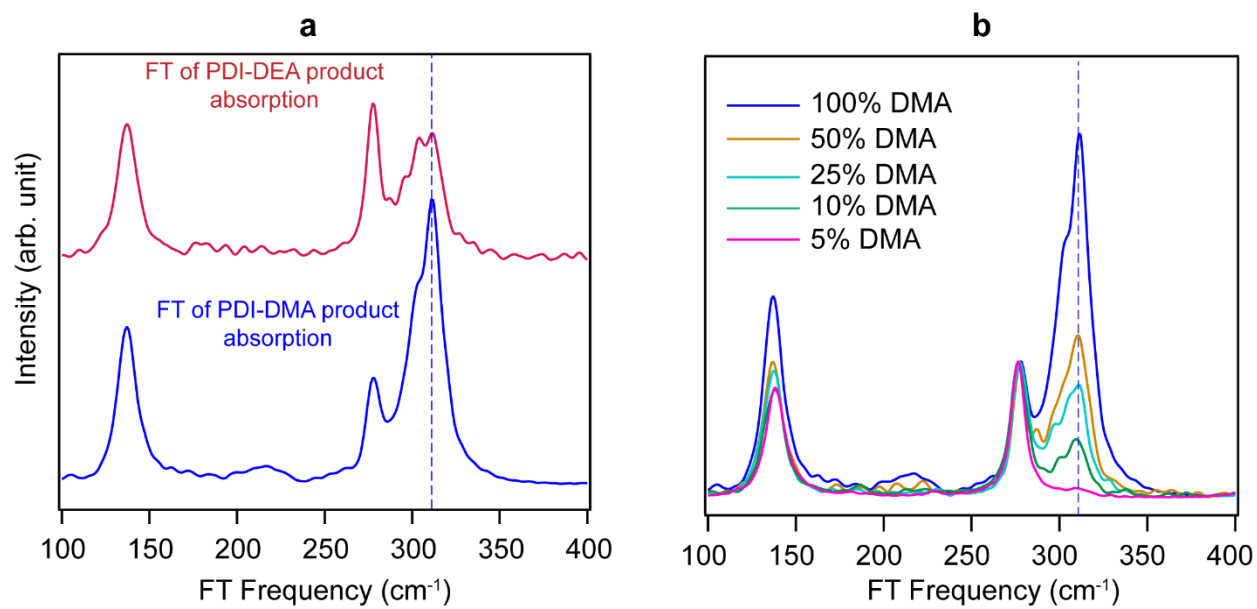
Figure 7| Coherent dynamics in the product absorption signals as a function of donor solvent. a, A comparison of FT spectra of the product state in PDI-DMA and PDI-DEA is shown. All the frequencies match completely. The 313 cm^{-1} peak is reproduced at the same frequency (with a decrease in amplitude) in diethylaniline as it was in dimethylaniline. **b,** The response of the 313 cm^{-1} mode was measured as a function of dilution of DMA with THF. The data is plotted by intensity normalizing the FT spectra to the 276 cm^{-1} peak.
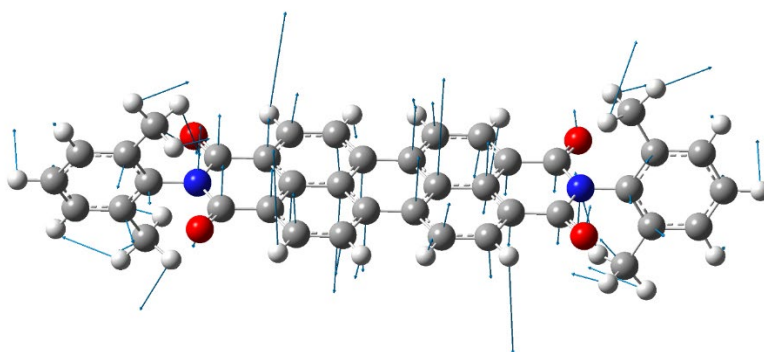
Figure 8| A candidate vibration from quantum calculations. Density functional theory calculations performed on PDI radical anion in the gas phase reveals a candidate vibration of frequency 319 cm^{-1} which is within the frequency range of the impulsively generated coherence on the ET product state. The *ab initio* calculations were performed using Gaussian 16 with the exchange-correlational functional PBE and basis function 6-311G*(d,p).[4]
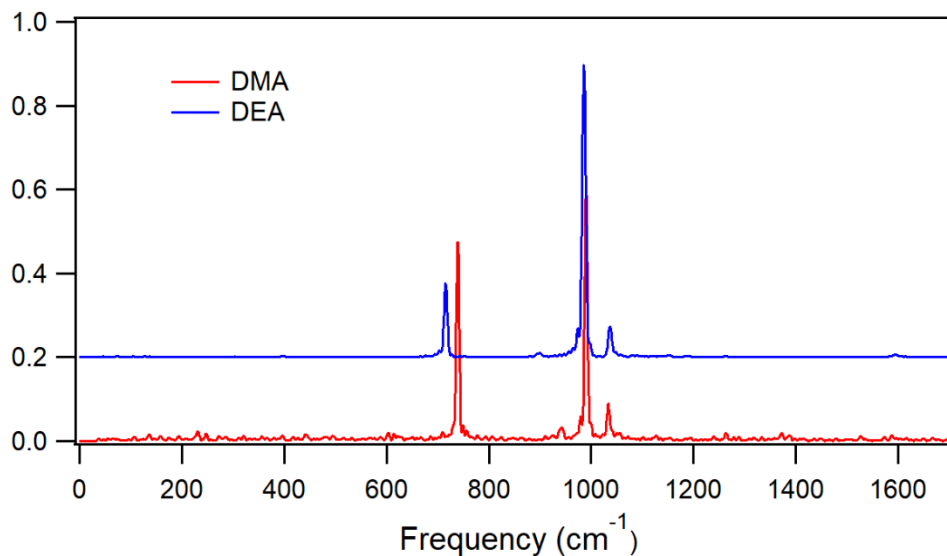
Figure 9| Impulsive stimulated Raman spectra of dimethylaniline and diethylaniline donor solvents. These spectra represent the impulsive stimulated Raman spectra of the two donor solvents. Both donor solvents have strong frequencies in the range of 600-1200 cm^{-1} and no frequency can be found in the region around 300 cm^{-1} frequency. The spectra were obtained by performing broadband pump-probe measurements of the two pure solvents under non-resonant conditions.
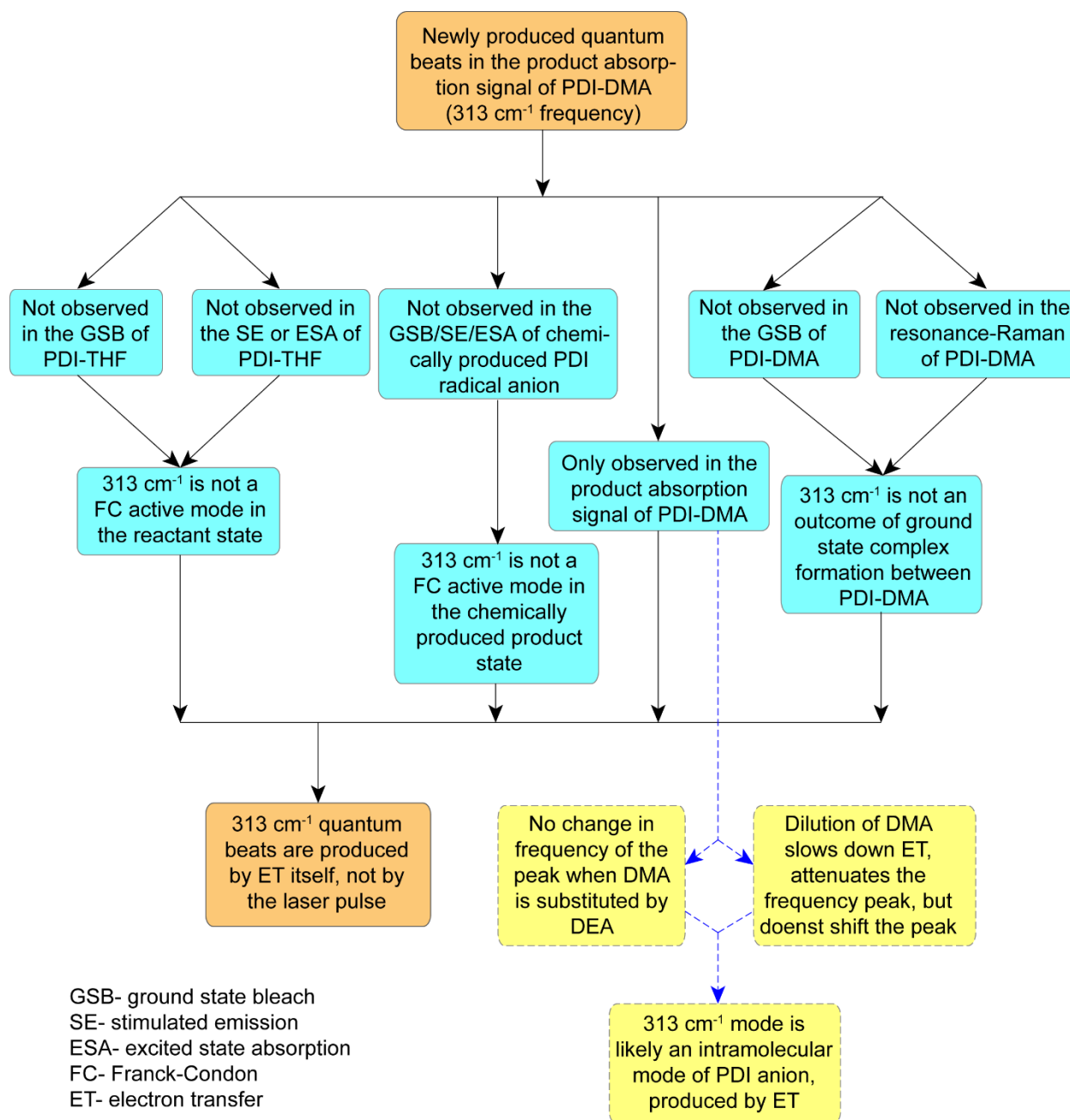
Scheme 1| Textual scheme of all the experimental controls. A textual scheme is illustrated that provides an overview of all the control experiments performed to confirm the mechanism behind the generation of the new wavepacket on the electron transfer product state.

Quantum Dynamics Simulations

Discussion based on the predictions of quantum dynamics simulations. The impulsive generation of a coherent wavepacket on a second coordinate of the product state is counter-intuitive, considering that our system has two orthogonal vibrational modes and the reactant state was prepared stationary along the low-frequency coordinate. However, the quantum dynamics simulations accompanying the experimental observation provide us with a clear physical insight. Because of a nonzero displacement along the low-frequency coordinate as well as the time period of this mode being longer than the time constant of electron transfer, the system is suddenly pushed out of equilibrium by the ultrafast ET reaction, thus incurring a subsequent nonstationary evolution of the low-frequency wavepacket on the product state. As depicted in Fig. 10, the classical description of the system, together with the assumption that the ET trajectory could be dissected into fast motions driven by the high-frequency vibration and slow motions driven by the low-frequency vibration, offers an alternative inspiring explanation. The classical particle suddenly transits to the product potential well after it goes across the curve crossing region, which leaves it out of equilibrium along both coordinates and thus leads to the subsequent oscillations. Coming back to the quantum mechanical point of view, from the perspective of vibrational wavepacket being regarded as a superposition of different vibrational levels, the low-frequency wavepacket is achieved by projecting the stationary low-frequency vibrational wavefunction of the reactant state onto the respective vibrational levels associated with the product state. Snapshots of wavepackets evolution illustrating the coherent vibrational dynamics along the high- and low-frequency modes before and after ET reaction are shown in Fig. 11. These illustrations depict that while the reactant state is prepared coherently along the high-frequency coordinate and thermally along the low-frequency coordinate, the ballistic electron transfer results in the impulsive generation of a coherence along the low-frequency coherence. The simulations thus confirm that the electron transfer reaction, under certain specific conditions, can spontaneously generate a low-frequency coherence on the product state, irrespective of whether the reactant state is prepared coherently or thermally along that mode. This finding suggests that ET-induced generation of vibrational coherence may exist in some other molecular systems as well, but the spectroscopic signature of this unique process may be shadowed by the wavepackets generated along Franck-Condon active modes of the reactant state. The reactive PDI-DMA system in this study turns to serve as an ideal platform for observing an exclusively ET-induced vibrational wavepacket.
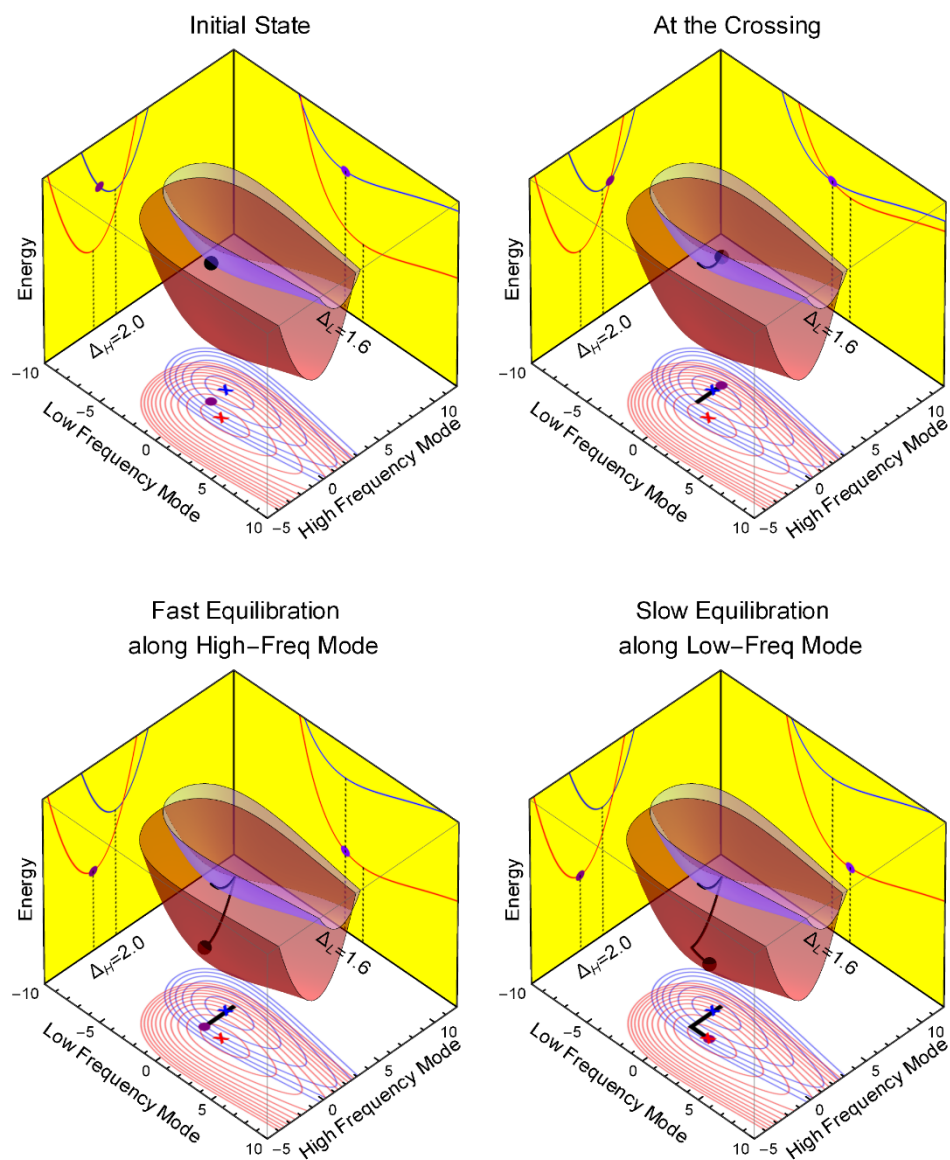
Figure 10| Proposed electron transfer trajectory along high- and low-frequency quantum modes. The proposed schematic electron transfer trajectory in terms of a classical particle is shown here as a function of two reaction coordinates. The time evolution of the dot on the two-dimensional reactant surface (blue) depicts that the system initially evolves preferentially along the high-frequency quantum coordinate till it encounters the curve crossing region. On the product surface (red), the system initially equilibrates along the high-frequency coordinate again, due to its shorter time-period. The system on the product state is simultaneously prepared at a nonequilibrium configuration along the low-frequency coordinate, therefore, the ballistic ET event generates a coherent wavepacket along the low-frequency coordinate. The system then equilibrates at the new, displaced position along the low-frequency coordinate.
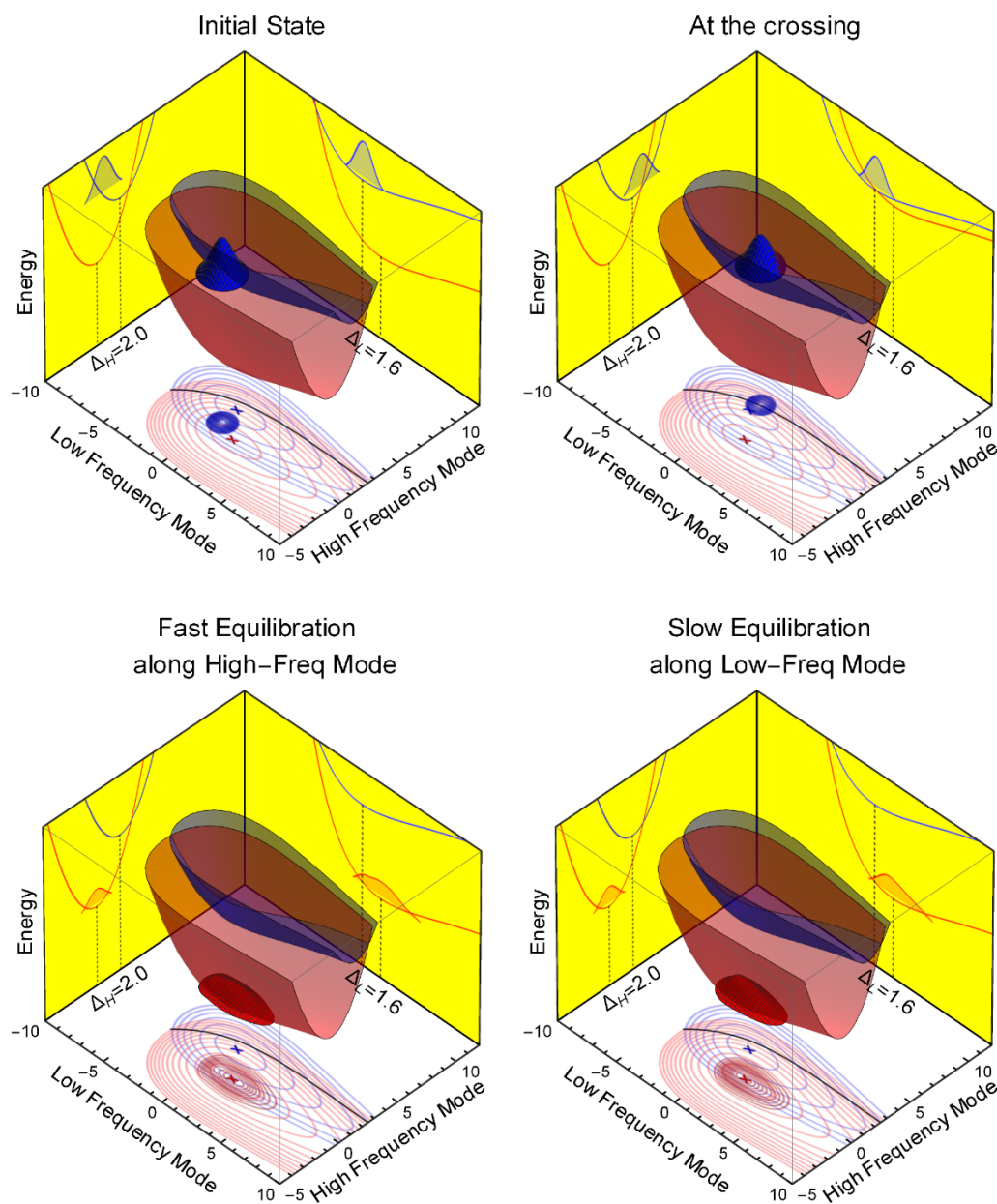
Figure 11| Wavepacket evolution along high- and low-frequency quantum modes. The time evolution of the wavepacket along the two reaction coordinates is depicted on the two-dimensional reactant and product potential energy surfaces. Four snapshots from a quantum dynamics simulation are chosen to illustrate the time instants when wavepacket is at the initial state, reaches the crossing for the first time, equilibrates along the fast high-frequency vibration and finally equilibrates along the slow low-frequency vibration.

Methodology of Quantum Dynamics Simulations

Model Hamiltonian. In order to apply the Redfield theory of quantum dissipative dynamics, we first partition the Hamiltonian of the total system $\hat{H}$ into the subsystem Hamiltonian $\hat{H}_S$, the system-bath interaction Hamiltonian $\hat{H}_{SB}$ and the thermal bath Hamiltonian $\hat{H}_B$

$$\hat{H} = \hat{H}_S + \hat{H}_{SB} + \hat{H}_B$$

The subsystem Hamiltonian considers the involved electronic states and vibrations explicitly as

$$\hat{H}_S = \sum_{i=G,R,P} \left(\epsilon_i + \frac{1}{2}\hbar\omega_L \hat{P}_L^2 + \frac{1}{2}\hbar\omega_H \hat{P}_H^2 + h_{i,L}(\hat{Q}_L) + h_{i,H}(\hat{Q}_H) \right) |i\rangle\langle i| - J|R\rangle\langle P| - J|P\rangle\langle R|$$

where three electronic states (ground state $|G\rangle$, reactant state $|R\rangle$ and product state $|P\rangle$) with energy levels $\{\epsilon_i\}$ and vibrational motions of two vibrational modes (a high-frequency mode labelled as "H" and a low-frequency mode labeled as "L") are treated explicitly, the constant electronic coupling J is here responsible for the charge transfer transition between reactant state $|R\rangle$ and product state $|P\rangle$, $\hat{P}_{H/L}$, $\hat{Q}_{H/L}$ and $\omega_{H/L}$ are respectively the momentum operator, the position operator and the frequency of the high/low frequency mode.

The potential energy surface (PES) associated with electronic state $|i\rangle$ is modelled along the high frequency mode as a harmonic potential

$$h_{i,H}(\hat{Q}_H) = \frac{1}{2}\hbar\omega_H(\hat{Q}_H - Q_H^{i0})^2$$

and along the low frequency mode as a Morse-type potential,

$$h_{i,L}(\hat{Q}_L) = D\left(1 - e^{-\beta(\hat{Q}_L - Q_L^{i0})}\right)^2$$

where $Q_{H/L}^{i0}$ are the equilibrium positions of the respective vibrational modes associated with electronic state $|i\rangle$, D is the dissociation energy of the Morse potential and $\beta = \sqrt{\hbar\omega_L/2D}$ determines the width of the Morse potential. Note that we here employ the dimensionless position operator $\hat{Q}_{L/H}$ and momentum operator $\hat{P}_{L/H}$ which relate to the real space position operators $\hat{q}_{L/H}$ and $\hat{p}_{L/H}$ as

$$\hat{q}_{L/H} = \ell_{L/H}\hat{Q}_{L/H}$$

$$\hat{p}_{L/H} = (\hbar/\ell_{L/H})\hat{P}_{L/H}$$

with $\ell_{L/H} = \sqrt{\dfrac{\hbar}{m_{L/H}\omega_{L/H}}}$ where m_L and m_H are the effective masses for low- and high-frequency vibrations.

The vibrational relaxations of both vibrational modes are modelled through the linear coupling of the system to their respective independent thermal bath as

$$\hat{H}_{SB} = \sum_{i=G,R,P} (\hat{Q}_L - Q_L^{i0})|i\rangle\langle i| \sum_\alpha \eta_{L,\alpha}\hat{q}_{L,\alpha} + \sum_{i=G,R,P} (\hat{Q}_H - Q_H^{i0})|i\rangle\langle i| \sum_\alpha \eta_{H,\alpha}\hat{q}_{H,\alpha}$$

with the thermal bath modelled as

$$\hat{H}_B = \sum_{j=L,H,\alpha} (\frac{1}{2}\hbar\omega_{j,\alpha}\hat{p}_{j,\alpha}^2 + \frac{1}{2}\hbar\omega_{j,\alpha}\hat{q}_{j,\alpha}^2)$$

where $\hat{p}_{H/L,\alpha}$, $\hat{q}_{H/L,\alpha}$ and $\omega_{H/L,\alpha}$ are respectively the position operator, momentum operator and frequencies of the bath mode α associated with high/low frequency vibrations.

We then carry out a unitary transformation, known as polaron transformation[5]

$$\hat{U} = \prod_{i=G,R,P} e^{-|i\rangle\langle i|\sum_{j=L,H} Q_j^{i0}\frac{\partial}{\partial\hat{Q}_j}}$$

which results in

$$\hat{H}_S' = \hat{U}\hat{H}_S\hat{U}^{-1} = \sum_{i=G,R,P} (\epsilon_i + \frac{1}{2}\hbar\omega_L\hat{P}_L^2 + \frac{1}{2}\hbar\omega_H\hat{P}_H^2 + D(1 - e^{-\beta\hat{Q}_L})^2 + \frac{1}{2}\hbar\omega_H\hat{Q}_H^2)|i\rangle\langle i|$$
$$- Je^{-|R\rangle\langle R|\sum_{\alpha=L,H} Q_\alpha^{R0}\frac{\partial}{\partial\hat{Q}_\alpha}}|R\rangle\langle P| e^{|P\rangle\langle P|\sum_{\alpha=L,H} Q_\alpha^{P0}\frac{\partial}{\partial\hat{Q}_\alpha}}$$
$$- Je^{-|P\rangle\langle P|\sum_{\alpha=L,H} Q_\alpha^{P0}\frac{\partial}{\partial\hat{Q}_\alpha}}|P\rangle\langle R|e^{|R\rangle\langle R|\sum_{\alpha=L,H} Q_\alpha^{R0}\frac{\partial}{\partial\hat{Q}_\alpha}}$$

and

$$\hat{H}_{SB} = \hat{U}\hat{H}_{SB}\hat{U}^{-1} = \sum_{i=G,R,P} \hat{Q}_L|i\rangle\langle i| \sum_\alpha \eta_{L,\alpha}\hat{q}_{L,\alpha} + \sum_{i=G,R,P} \hat{Q}_H |i\rangle\langle i| \sum_\alpha \eta_{H,\alpha}\hat{q}_{H,\alpha}$$

With the help of the polaron transformation, we are able to recast the Hamiltonian in terms of the electronic-vibrational states $|i, \nu_H, \nu_L\rangle = |i\rangle\otimes|\nu_H(Q_H^{i0})\rangle \otimes|\nu_L(Q_L^{i0})\rangle$ with $|\nu_{H/L}(Q_{H/L}^{i0})\rangle$ representing a high/low frequency displaced oscillator state with the equilibrium position $Q_{L/H}^{i0}$ of electronic state $|i\rangle$, which results in

$$\hat{H}_S' = \sum_{i=G,R,P} \sum_{n_L,n_H} \left(\epsilon_i + \hbar\omega_H(n_H + \frac{1}{2}) + \hbar\omega_L\left[\left(n_L + \frac{1}{2}\right) - \chi_e\left(n_L + \frac{1}{2}\right)^2\right]\right) |i, n_L, n_H\rangle \langle i, n_L, n_H|$$
$$+ \sum_{n_L,n_H} \sum_{n_L',n_H'} M_{n_L n_L'}^{MO}(Q_L^{R0} - Q_L^{P0}) M_{n_H n_H'}^{HO}(Q_H^{R0} - Q_H^{P0}) J|R, n_L, n_H\rangle \langle P, n_L', n_H'|$$
$$+ \sum_{n_L,n_H} \sum_{n_L',n_H'} M_{n_L n_L'}^{MO}(Q_L^{P0} - Q_L^{R0}) M_{n_H n_H'}^{HO}(Q_H^{P0} - Q_H^{R0}) J|P, n_L, n_H\rangle \langle R, n_L', n_H'|$$

The overlap between vibrational wavefunctions is also called Franck-Condon factor and calculated respectively for harmonic oscillator (HO) and Morse-type oscillator (MO)[6] as

$$M_{\nu_a \nu_b}^{HO}(Q_a - Q_b)$$

$$= \langle \nu_a(Q_a)|\nu_b(Q_b)\rangle|_{HO}$$

$$= [\text{sgn}(\nu_a - \nu_b)]^{\nu_b - \nu_a} \left(\frac{Q_a - Q_b}{\sqrt{2}}\right)^{|\nu_a - \nu_b|} e^{-\frac{(Q_a - Q_b)^2}{4}} \left(\frac{\nu_{min}!}{\nu_{max}!}\right)^{\frac{1}{2}} L_{\nu_{min}}^{|\nu_a - \nu_b|}\left(\frac{(Q_a - Q_b)^2}{2}\right)$$

$$M_{\nu_a \nu_b}^{MO}(Q_a - Q_b) =$$

$$\langle v_a(Q_a)|v_b(Q_b)\rangle|_{\mathrm{MO}} = 2\sqrt{\frac{v_a! \, v_b! \, (j_a - v_a) \, (j_b - v_b)}{\Gamma(2j_a - v_a + 1)\Gamma(2j_b - v_b + 1)}} \, y_a^{j_a - v_a} y_b^{j_b - v_b}$$

$$\sum_{l_a, l_b = 0}^{v_a, v_b} \frac{(-1)^{l_a + l_b}}{l_a! \, l_b!} \binom{2j_a - v_a}{v_a - l_a} \binom{2j_b - v_b}{v_b - l_b} y_a^{l_a} y_b^{l_b} \left(\frac{2}{y_a + y_b}\right)^\alpha \Gamma(\alpha)$$

where we have $\beta_a = \beta_b$, $\alpha = j_a - v_a + l_a + j_b - v_b + l_b$ and

$$y_a = (2j_a + 1)e^{-\beta_a(Q_b - Q_a)/2}$$

$$y_b = (2j_b + 1)e^{+\beta_b(Q_b - Q_a)/2}$$

In order to evaluate the system-bath interaction $\widehat{H}_{SB}$, the vibrational matrix elements of the position operators are given respectively for harmonic and Morse oscillators[6,7] as

$$\langle \mu|\widehat{Q}_H|v\rangle = \frac{1}{\sqrt{2}}\left(\sqrt{v+1}\,\delta_{\mu,v+1} + \sqrt{v}\,\delta_{\mu,v-1}\right)$$

$$\langle m|\widehat{Q}_L|n\rangle = \sqrt{k/2}\,\frac{(-1)^{n-m+1}}{(n-m)(k-n-m-1)}\left[\frac{n!}{m!}\frac{\Gamma(k-n)}{\Gamma(k-m)}(k-2n-1)(k-2m-1)\right]^{\frac{1}{2}} \quad (n > m)$$

where $k = 4D/\hbar\omega_L$.

Redfield Theory

The reduced density operator is defined as

$$\hat{\sigma}(t) = \mathrm{Tr}_{\mathrm{B}}\{\hat{\rho}(t)\}$$

where $\hat{\rho}(t)$ denotes the density operator of the total system and $\mathrm{Tr}_{\mathrm{B}}\{\cdots\}$ averages over the bath degrees of freedom. The time evolution of the subsystem then follows[8,9]

$$\frac{d\hat{\sigma}}{dt} = -\frac{i}{\hbar}[\widehat{H}_S, \hat{\sigma}] + \widehat{\mathcal{R}}\,\hat{\sigma}$$

where $\widehat{\mathcal{R}}$ is the Redfield tensor whose matrix element in terms of eigenstate basis is

$$\mathcal{R}_{ij,kl} = -\frac{1}{\hbar^2}\int_0^\infty d\tau\,[\langle(H_{SB})_{lj}(0)(H_{SB})_{ik}(\tau)\rangle e^{-i\omega_{lj}\tau} + \langle(H_{SB})_{lj}(\tau)(H_{SB})_{ik}(0)\rangle e^{-i\omega_{ik}\tau}$$

$$-\delta_{lj}\sum_s \langle(H_{SB})_{is}(\tau)(H_{SB})_{sk}(0)\rangle e^{-i\omega_{sk}\tau} - \delta_{ki}\sum_s \langle(H_{SB})_{ls}(0)(H_{SB})_{sj}(\tau)\rangle e^{-i\omega_{ls}\tau}],$$

where $\langle\cdots\rangle = Tr_B\{\hat{\rho}_B\cdots\}$ averages over the bath degrees of freedom. In order to reduce the computation cost, we employ the Hilbert space representation.[9] Given that the system-bath interaction could be recast as products of the system operator $\widehat{K}_a$ and bath operator $\widehat{\Phi}_a$, i.e.,

$$\widehat{H}_{SB} = \sum_a \widehat{K}_a \widehat{\Phi}_a$$

one can recast the Redfield master equation as

$$\frac{d}{dt}\hat{\sigma}(t) = -\frac{i}{\hbar}[\hat{H}_S,\hat{\sigma}] + \frac{1}{\hbar^2}\sum_a\left([\hat{K}_a^+\hat{\sigma}(t),\hat{K}_a] + [\hat{K}_a,\hat{\sigma}(t)\hat{K}_a^-]\right)$$

where operators $\hat{K}_a^+$ and $\hat{K}_a^-$ are defined as

$$\left(\hat{K}_a^+\right)_{ij} = \sum_b\left(\hat{K}_b\right)_{ij}(\Theta_{ab}^+)_{ij}$$

$$\left(\hat{K}_a^-\right)_{ij} = \sum_b\left(\hat{K}_b\right)_{ij}(\Theta_{ba}^-)_{ij}$$

along with

$$(\Theta_{ab}^+)_{ij} = \int_0^\infty d\tau\, e^{-i\omega_{ij}\tau}\left\langle\hat{\Phi}_a(\tau)\hat{\Phi}_b(0)\right\rangle_B = \frac{1}{2}S_{ab}^+(\omega_{ji}) + i\lambda_{ab}^+(\omega_{ji})$$

$$(\Theta_{ab}^-)_{ij} = \int_0^\infty d\tau\, e^{-i\omega_{ij}\tau}\left\langle\hat{\Phi}_a(0)\hat{\Phi}_b(\tau)\right\rangle_B = \frac{1}{2}S_{ab}^-(\omega_{ji}) + i\lambda_{ab}^-(\omega_{ji})$$

$$= \frac{1}{2}S_{ab}^+(\omega_{ij}) + i\lambda_{ab}^+(\omega_{ij})$$

where $\langle\cdots\rangle_B = Tr_B\{\hat{\rho}_B\cdots\}$, $\left\langle\hat{\Phi}_a(\tau)\hat{\Phi}_a(0)\right\rangle_B$ is autocorrelation function, $\left\langle\hat{\Phi}_a(\tau)\hat{\Phi}_b(0)\right\rangle_B (a\neq b)$ is cross-correlation function and the Fourier transform of the autocorrelation function is then given as

$$S_{ab}^+(\omega) = \int_{-\infty}^\infty d\tau\, e^{i\omega\tau}\left\langle\hat{\Phi}_a(\tau)\hat{\Phi}_b(0)\right\rangle_B$$

$$S_{ab}^-(\omega) = \int_{-\infty}^\infty d\tau\, e^{i\omega\tau}\left\langle\hat{\Phi}_a(0)\hat{\Phi}_b(\tau)\right\rangle_B = \int_{-\infty}^\infty d\tau\, e^{-i\omega\tau}\left\langle\hat{\Phi}_a(\tau)\hat{\Phi}_b(0)\right\rangle_B = S_{ab}^+(-\omega)$$

We drop the cross-correlation functions by assuming independent thermal bath $\{\hat{\Phi}_a\}$. The imaginary part of the noise-power spectrum is also dropped for simplicity, because they are only significant for low temperature dynamics. Finally, we have

$$\left(\hat{K}_a^+\right)_{ij} = \frac{1}{2}\left(\hat{K}_a\right)_{ij}S_{aa}^+(\omega_{ji})$$

$$\left(\hat{K}_a^-\right)_{ij} = \frac{1}{2}\left(\hat{K}_a\right)_{ij}S_{aa}^+(\omega_{ij})$$

In our simulation, the noise-power spectrum $S_{aa}^+(\omega)$ is

$$S_{aa}^+(\omega) = S_{aa}^-(-\omega) = J_a(\omega)(n(\omega) + 1)$$

where $n(\omega) = \left(e^{\hbar\omega/k_BT} - 1\right)^{-1}$ is the Bose-Einstein distribution function and the spectra density of the thermal bath takes the Ohmic form,

$$J_a(\omega) = \eta_a\omega e^{-|\omega|/\omega_{c\alpha}}$$

with η_a a dimensionless damping constant and ω_{ca} the cut-off frequency for thermal bath a.

Initial Wavepackets

For simplicity and clear physical picture, we set up the initial photo-excited wavepacket by projecting the static wavefunction of ground state to reactant state potential energy surface. Given the static wavefunction of ground state $|v(Q^{G0}) = 0\rangle$, the wave packet generated on the reactant state will be $\sum_v c_v |v(Q^{R0})\rangle$ with $c_v = \langle v(Q^{R0})|v(Q^{G0}) = 0\rangle$. Therefore, the initial wavepacket that is nonstationary along the high-frequency mode but stationary along the low-frequency mode is given as

$$|\psi_{\text{init}}\rangle = |R\rangle \otimes \sum_{v_H} c_{v_H} |v_H(Q_H^{R0})\rangle \otimes |v_L(Q_L^{P0}) = 0\rangle$$

with

$$c_{v_H} = \langle v_H(Q_H^{R0})|v_H(Q_H^{G0}) = 0\rangle.$$

When the initial wavepacket is prepared nonstationary on both high-frequency and low-frequency coordinates, it is characterized by

$$|\psi_{\text{init}}\rangle = |R\rangle \otimes \sum_{v_H} c_{v_H} |v_H(Q_H^{R0})\rangle \otimes \sum_{v_L} c_{v_L} |v_L(Q_L^{R0}) = 0\rangle$$

where

$c_{v_L} = \langle v_L(Q_L^{R0})|v_L(Q_L^{G0}) = 0\rangle.$

Parameters

The parameters $J = 400 \text{ cm}^{-1}$, $\epsilon_R - \epsilon_P = 6000 \text{ cm}^{-1}$, $\omega_L = 320 \text{ cm}^{-1}, \omega_H = 1600 \text{ cm}^{-1}$, $D = 7223 \text{ cm}^{-1}$, $\beta = 0.15$, $\eta_H = 0.74, \eta_L = 0.02, \omega_{cH} = 2000 \text{ cm}^{-1}, \omega_{cL} = 500 \text{ cm}^{-1}$ are used in all simulations presented in the main text.

The equilibrium minima of respective electronic states vary in different simulations:

1) The simulations with initial wavepacket prepared nonstationary along high-frequency mode and stationary along low-frequency mode adopt $(Q_H^{G0}, Q_L^{G0}) = (0,0)$, $(Q_H^{R0}, Q_L^{R0}) = (1.4,0)$, $Q_H^{P0} = -0.6, Q_L^{P0} = 0,1.6,2.0,2.4$.
2) The simulations with initial wavepacket prepared nonstationary along both coordinates adopts $(Q_H^{G0}, Q_L^{G0}) = (0,0)$, $(Q_H^{R0}, Q_L^{R0}) = (1.4,1.4)$, $(Q_H^{P0}, Q_L^{P0}) = (-0.60,3.0)$.
3) The simulation for the wavepacket evolution presented in Figure 4 adopts $(Q_H^{G0}, Q_L^{G0}) = (0,0)$, $(Q_H^{R0}, Q_L^{R0}) = (1.4,0)$, $(Q_H^{P0}, Q_L^{P0}) = (3.6,1.6)$, the energy gap is here adjusted to $\epsilon_R - \epsilon_P = 3000 \text{ cm}^{-1}$ for a better view of the adiabatic potential energy surface.

Simulation Details

In our simulation, we characterize the quantum dynamics of the studied system by calculating the expectation values of the following operators as a function of time:

(1) the electronic populations $\hat{P}_R = |R\rangle\langle R| \otimes \mathbb{I}_L \otimes \mathbb{I}_H$, $\hat{P}_P = |P\rangle\langle P| \otimes \mathbb{I}_L \otimes \mathbb{I}_H$,

(2) the wavepacket amplitude along high-frequency mode $\hat{Q}_H^R = |R\rangle\langle R|\otimes\hat{Q}_H\otimes\mathbb{I}_L$, $\hat{Q}_H^P = |P\rangle\langle P|\otimes\hat{Q}_H\otimes\mathbb{I}_L$,

(3) the wavepacket amplitude along low-frequency mode, $\hat{Q}_L^R = |R\rangle\langle R|\otimes\mathbb{I}_H\otimes\hat{Q}_L$, $\hat{Q}_L^P = |P\rangle\langle P|\otimes\mathbb{I}_H\otimes\hat{Q}_L$.

The visualization of the wavepacket evolution presented in Figure 4 is achieved by computing the nuclear density associated with the reactant and product states. Given the density matrix blocks corresponding to reactant and product states as

$$\hat{\rho}^i = \sum_{\substack{v_H,v_L \\ v_H',v_L'}} c^i_{v_H v_L, v_H' v_L'} |i\rangle\otimes|v_H(Q_H^{i0})\rangle\otimes|v_L(Q_L^{i0})\rangle \langle i|\otimes\langle v_H'(Q_H^{i0})|\otimes\langle v_L'(Q_H^{i0})|$$

the nuclear density of respective electronic states is computed as

$$\rho^i(\boldsymbol{Q}) = Tr\{\hat{\rho}^i|\boldsymbol{Q}\rangle\langle\boldsymbol{Q}|\} = \sum_{\substack{v_H,v_L \\ v_H',v_L'}} c^i_{v_H v_L, v_H' v_L'} \phi_{v_L}^L(Q_L - Q_L^{i0})\phi_{v_H}^H(Q_H - Q_H^{i0})\phi_{v_L'}^L(Q_L - Q_L^{i0})\phi_{v_H'}^H(Q_H - Q_H^{i0})$$

where $|\boldsymbol{Q}\rangle$ with $Q = (Q_H, Q_L)$ is the real space basis, the label i refers to R (reactant state) or P (product state), $\phi_{v_H}^H(Q_H - Q_H^{i0})$ and $\phi_{v_L}^L(Q_L - Q_L^{i0})$ are respectively the eigenstate wavefunction of harmonic oscillator and Morse oscillator, i.e.,

$$\phi_v^H(Q_H - Q_H^{i0}) = \frac{1}{\sqrt{2^v n!}}\pi^{-\frac{1}{4}}e^{-\frac{(Q_H-Q_H^{i0})^2}{2}}H_v(Q_H - Q_H^{i0})$$

$$\phi_v^L(Q_L - Q_L^{i0}) = \sqrt{\frac{\beta v!\, 2(j-v)}{\Gamma(2j-v+1)}}e^{-\xi/2}\xi^{j-v}L_v^{2(j-v)}(\xi)$$

with

$$j = \left|\frac{2D}{\omega_L} - 0.5\right|$$

$$\xi = (2j+1)e^{-\beta(Q_L - Q_L^{i0})}$$

$$L_v^\alpha(\xi) = \sum_k^v \frac{(-1)^k\Gamma(v+\alpha+1)}{k!\,(v-k)!\,\Gamma(k+\alpha+1)}\xi^k$$

$$H_v(z) = (-1)^v e^{z^2}\frac{d^v}{dz^v}(e^{-z^2})$$

The adiabatic potential energy surface presented in Figure 4 is obtained by diagonalizing the electronic Hamiltonian as

$$\begin{pmatrix} h_H^R(Q_H) + h_L^R(Q_L) & -J \\ -J & h_H^P(Q_H) + h_L^P(Q_L) \end{pmatrix}\begin{pmatrix}\Psi_1(Q_H,Q_L) \\ \Psi_2(Q_H,Q_L)\end{pmatrix} = \begin{pmatrix}E_1(Q_H,Q_L) & 0 \\ 0 & E_2(Q_H,Q_L)\end{pmatrix}\begin{pmatrix}\Psi_1(Q_H,Q_L) \\ \Psi_2(Q_H,Q_L)\end{pmatrix}$$

where $\Psi_1(Q_H,Q_L)$ and $\Psi_2(Q_H,Q_L)$ are adiabatic state wavefunctions, $E_1(Q_H,Q_L)$ and $E_2(Q_H,Q_L)$ are adiabatic state potential energy surfaces.

In all simulations, the Redfield master equation is solved for 12 ps through numerical integration with a time step of 0.10 fs.

References

1. McClure, S. D., Turner, D. B., Arpin, P. C., Mirkovic, T. & Scholes, G. D. Coherent Oscillations in the PC577 Cryptophyte Antenna Occur in the Excited Electronic State. *J. Phys. Chem. B* **118**, 1296-1308 (2014).
2. Liebel, M., Schnedermann, C., Wende, T. & P, K. Principles and Applications of Broadband Impulsive Vibrational Spectroscopy. *J. Phys. Chem. A* **119** (2015).
3. Rather, S. R. & Scholes, G. D. Slow Intramolecular Vibrational Relaxation Leads to Long-Lived Excited-State Wavepackets. *J. Phys. Chem. A* **120**, 6792-6799 (2016).
4. Frisch, M. J. *et al. Gaussian 09, Revision C.01.* (2010).
5. Nitzan, A. *Chemical dynamics in condensed phases : relaxation, transfer and reactions in condensed molecular systems. Oxford graduate texts* (Oxford University Press, 2006).
6. Lopez, J. C., Rivera, A. L., Smirnov, Y. F. & Frank, A. Simple evaluation of Franck-Condon factors and non-Condon effects in the Morse potential. *International Journal of Quantum Chemistry* **88**, 280-295 (2002).
7. Zuniga, J. *et al.* Analytical Expressions for Vibrational Matrix-Elements of Morse Oscillators. *Physical Review A* **38**, 4205-4212 (1988).
8. Jean, J. M. & Fleming, G. R. Competition between Energy and Phase Relaxation in Electronic Curve Crossing Processes. *J. Chem. Phys.* **103**, 2092-2101 (1995).
9. Pollard, W. T., Felts, A. K. & Friesner, R. A. The Redfield equation in condensed-phase quantum dynamics. *Advances in Chemical Physics, Vol Xciii* **93**, 77-134 (1996).